



# Experimental and Computational Investigation of Mass Injection Induced Unstart

Jeffrey A. Fike\*, Karthik Duraisamy† and Juan J. Alonso‡

*Department of Aeronautics and Astronautics  
 Stanford University, Stanford, CA 94305*

Hyungrok Do§, Seong-kyun Im¶ and Mark A. Cappelli||

*Department of Mechanical Engineering  
 Stanford University, Stanford, CA 94305*

Jet injection into a confined supersonic cross flow is studied using experiments and numerical simulations, with the goal of identifying the conditions that cause the flow to unstart. This is accomplished by varying the jet momentum ratio and studying the evolution of the complex pattern of shocks and shock-boundary layer interactions that ultimately lead to unstart. Reynolds-Averaged Navier-Stokes simulations and experimental data (Planar Laser Rayleigh Scattering) are used to identify the upstream location of the shock system, and the distance between this location and the inlet is used to define the safety margin. A preliminary investigation is performed on the sensitivities of the unstart margin to various uncertainties associated with the geometry and flow conditions of the experiment, as well as the choice of turbulence model in the simulations. This work reports initial progress towards the larger goal of quantifying margins and uncertainties in scramjet unstart and also evaluates the ability of steady RANS simulations to predict precursor conditions leading to the highly unsteady unstart process.

## Nomenclature

$\rho$	fluid density
$u$	fluid velocity magnitude
$M$	fluid Mach number
$P$	fluid pressure
$T$	fluid temperature
$\gamma$	ratio of specific heats for the fluid
$R$	square root of the jet momentum ratio
$L_{Mach\ disk}$	location of the Mach disk relative to the jet exit
$d_{jet}$	diameter of the jet exit
$h$	half width/height of the tunnel

### Subscripts:

$\infty$	nominal conditions of the cross flow
<i>jet</i>	conditions at the jet exit
<i>plenum</i>	conditions in the jet plenum
0	stagnation quantities

\*Graduate Student, AIAA Student Member.

†Consulting Assistant Professor, AIAA Member.

‡Associate Professor, AIAA Member.

§Post Doctoral Scholar.

¶Graduate Student, AIAA Student Member.

||Professor.

# I. Introduction

Although hypersonic propulsion systems have been postulated for many years, recent successes in experimental demonstrations of hypersonic air-breathing vehicles such as the Hyshot,<sup>1</sup> X-43A<sup>2</sup> and X-51A<sup>3</sup> vehicles, and upcoming demonstrations as part of the HIFiRE<sup>4-6</sup> program are highlighting the need for predictive tools that can one day help realize scramjet engines for hypersonic vehicles of various kinds. Because of the nature of the speed regime, hypersonic propulsion systems operate close to a number of failure boundaries that result from fluid mechanical, structural, and heat transfer constraints.

The performance of a scramjet engine is tuned to achieve the highest level of thrust that is compatible with a specified safety margin, which is typically defined as the interval in a particular metric between the nominal design conditions and critical failure. An important mode of failure associated with scramjet engines is unstart, where the scramjet engine is unable to support the level of mass flow or heat addition required and a complex pattern of shock waves forms and propagates upstream (typically beyond the hypersonic inlet) until the engine loses virtually all of its mass flow and operating thrust. Unstart events in hypersonic systems are typically catastrophic and can lead to system failure and, possibly, loss of mission.

A typical scramjet functions by compressing incoming supersonic air in the inlet/isolator through a sequence of oblique shocks. The flow is still supersonic when it reaches the combustor section of the engine. At this point, fuel is injected and combustion occurs to increase the energy of the flow. This high energy mixture is expanded through a nozzle to generate useful thrust. Under certain conditions and depending on the amount of heat addition, the injection and combustion of fuel can create large regions of subsonic flow in the combustor, leading to a potentially catastrophic situation where the shock system can propagate upstream and reach the inlet plane. Such situations are described as unstart caused by heat addition or thermal choking. As mentioned earlier, for aircraft powered by a scramjet engine, unstart can be a catastrophic occurrence as the vehicle can experience a dramatic increase in drag, a loss of thrust, and the inability to control the flight path of the vehicle. Avoiding unstart is therefore critical to the design and operation of a scramjet engine.

Among other factors, unstart can be initiated either by thermal choking<sup>7</sup> or changes in stoichiometry of the mixture or simply by excessive blockage at the injector and subsequent flow separation. In this work, an investigation of margins and uncertainties in mass-injection induced unstart is performed and the results presented herein are for a single jet of air injected into a supersonic flow of air within the confines of a simulated isolator/combustor.

The highly-complicated, multi-physics nature of the associated flow phenomena means that predictive simulations will involve multiple uncertainties resulting from an improper knowledge of the operating conditions or from poor modeling assumptions. Because of the high impact of these aleatory (uncertainties resulting from natural variability in flow conditions, heat addition, combustion details, and geometry of the engine) and epistemic (uncertainties resulting from the lack of modeling that is present in numerical simulations of the flow within scramjets) uncertainties, careful accounting of the effects of these uncertainties on the margins (rather than just on the details of the flow) should be performed if confidence is to be placed on predictive tools.

The goal of this paper is thus not simply to validate the simulations so that we can accurately predict when unstart will occur, but to quantify the effect of the errors and uncertainties inherent in the simulation on the prediction of the unstart margins. The ultimate goal, of which the present work is a first step, is to ensure that uncertainty quantification methodologies are feasible within the context of high-fidelity simulations and that, in the process of developing new systems, a judicious investment of resources is pursued to balance the requirements of better modeling techniques, finer computational meshes, more effective sampling techniques, and, finally, more targeted use of experiments so that, jointly, hypersonic systems can be created with sufficient confidence so that they can be safely operated under a variety of conditions.

Section II describes the experimental and computational setup that we have used to pursue these investigations. Section III is a validation of the experimental and computational results in order to lend some confidence to our predictive methodologies. Section IV investigates a number of sources of uncertainty for the problem at hand, including the knowledge of flow conditions, the knowledge of the actual geometry of the experiment, and the knowledge of the actual physics of the flow. In section V we draw conclusions from the work presented and describe a number of ideas that we intend to pursue as part of our future work.

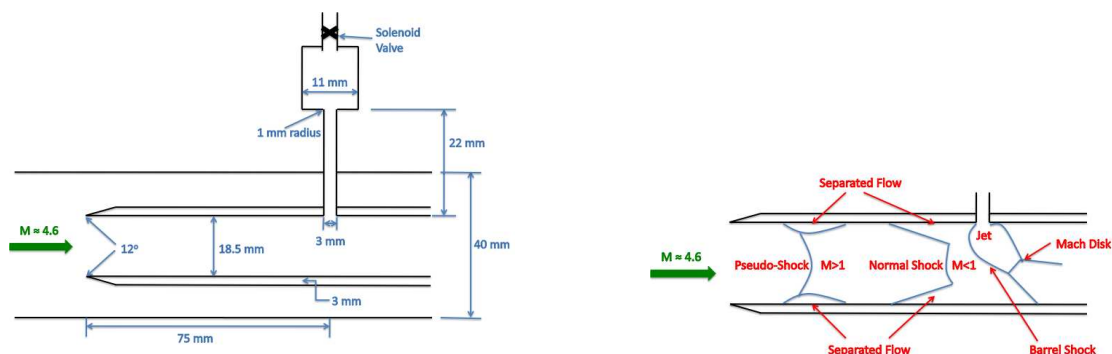
## II. System Description

For this study, a simplified geometry is used as an analog for a scramjet isolator/combustor. This study is also limited to non-reacting flows. The problem of fuel injection inside a scramjet is therefore idealized as an under-expanded sonic jet injected into a confined supersonic cross flow. The jet initiates a highly complex quasi-steady shock system that, under certain conditions, propagates upstream beyond the inlet plane and causes unstart, thus enabling us to specifically study unstart induced by mass injection. The characteristics of the jet are controlled by varying the pressure in the plenum.

The test section used for both the experiments and simulations has a 4 cm x 4 cm square cross-section. Splitter plates that span the entire width of the test section are used to vary the geometry being studied. Figure 1(a) shows the configuration that is being studied. The splitter plates are 3 mm thick and have a 12° wedged tip on one side. The tips of the splitter plates define the inlet for this model of a scramjet isolator. Several configurations are possible by varying the position and orientation of the splitter plates. These different configurations enable the isolation and study of the effect of boundary layer thickness and the presence of an oblique shock train prior to unstart.<sup>8</sup>

The results presented here are for two splitter plates spaced 18.5 mm apart with the wedged tips facing outward. This configuration is chosen to produce a flow that is free from a strong oblique shock train and has boundary layers that originate at the leading edges of the splitter plates. In this configuration, the splitter plates isolate the inlet flow from the boundary layers along the top and bottom of the tunnel. The sidewall boundary layer, however, is still present. The jet is injected at a right angle into a flow that is nominally at Mach 4.6 between the splitter plates. The jet exit has a diameter of 3 mm and the diameter of the plenum is nominally 11 mm. The tips of the splitter plates are 75 mm upstream from the center of the jet, and 270 mm downstream from the throat of the converging/diverging nozzle, which is not depicted in the figures.

The jet is initially turned off, by closing a valve upstream of the plenum, so that an undisturbed supersonic flow can be created between the splitter plates. Once this flow has been established, the valve is opened pressurizing the plenum and creating a jet that exhausts at a right angle into the supersonic crossflow between the splitter plates. The jet creates a blockage in the flow, causing a complex shock/flow separation system, as sketched in Fig. 1(b). The position and configuration of this shock system is dependent on the amount of blockage in the flow. Below some critical value of the plenum pressure, the shock system reaches a quasi-stationary position and remains downstream of the splitter plate tips. As the strength of the jet is increased, the blockage increases and the shock system moves further upstream. At some critical point, the shock moves upstream past the inlet defined by the splitter plate tips. When this occurs, the system is considered to have unstarted. Although many definitions of unstart can be used, this is the one we have pursued in this work as it can be easily quantified for constructing different metrics that cause unstart. It has to be mentioned that the same metric has been used to define a safety margin in the HIFiRE-2<sup>4,5</sup> tests.



(a) A schematic diagram showing the configuration being studied both experimentally and computationally.

(b) A sketch showing the basic flow features of the system at a jet pressure below the unstart threshold.

**Figure 1. Diagrams showing the configuration and basic flow features of the system. Nominally Mach 4.6 flow is present from left to right.**

The primary objective of this study is not to determine the critical point for unstart, but to predict, in some sense, how close the system is to unstating. For this study, the location of the leading shock is determined for various strength jets. The shock location plotted versus jet strength is referred to as an unstart margin curve. The unstart margin curve and knowledge of the unstart boundary for the system allow us to quantify how close the system is to unstating. When examining the effects of errors and uncertainties, it is not their impact on the details of the flow that we are interested in, it is how they affect the unstart margin.

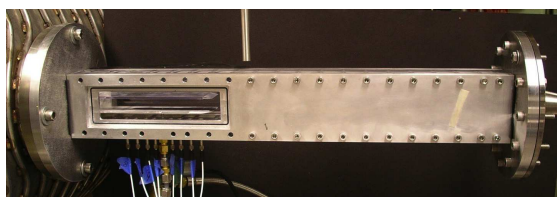
The strength of the jet is controlled by changing the plenum pressure. Throughout this report, the strength of the jet will be characterized by the plenum pressure. An alternative way of characterizing the strength of the jet is to compare it to the crossflow using the square root of the jet momentum ratio,<sup>9</sup>

$$R = \sqrt{\frac{(\rho u^2)_{jet}}{(\rho u^2)_{\infty}}} = \sqrt{\frac{(\gamma P M^2)_{jet}}{(\gamma P M^2)_{\infty}}}. \quad (1)$$

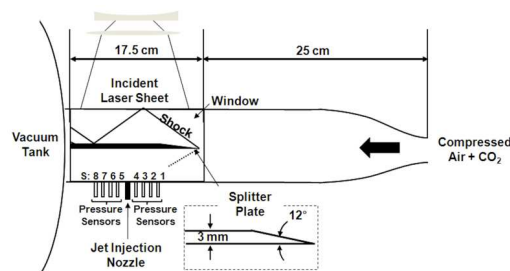
The jet momentum ratio allows comparisons to be made for different crossflow conditions. This is analogous to the equivalence ratio,  $\phi$ , which is often used when dealing with combustion to relate the mass flow of fuel to the mass flow of air.

## II.A. Details of the Experiment

The experiment is carried out using a nominally Mach 5 indraft wind tunnel, an integrated laser system and a jet injection module. The wind tunnel is shown in Fig. 2(a). A schematic of the Mach 5 wind tunnel, set up for an alternate configuration with only one splitter plate, is shown in Fig. 2(b). High-pressure air ( $P_0 = 350$  kPa and  $T_0 = 300$  K) containing carbon dioxide ( $\text{CO}_2$ ) (approximately 25% by volume) expands through a converging/diverging nozzle (25:1 area ratio) to establish a relatively uniform flow in a rectangular test section (4 cm  $\times$  4 cm cross-sectional area). A detailed characterization of the variation in Mach number of the flow across the test section is carried out by measuring the shock angle from a sharp leading 12° wedge using Schlieren photography. The measured Mach number at the centerline of the tunnel is  $M = 4.6$ , with a 5% variation wall to wall excluding the boundary layers, which were not resolved. The exit of the tunnel is connected to a vacuum tank that accommodates the incoming mass flow for approximately 5 seconds of run time. During this run time, the vacuum tank pressure is maintained at values lower than the static pressure in the test section. A honeycomb of 3 mm hexagonal cells 2.5 cm in length is placed upstream of the converging nozzle to suppress flow swirling, mostly generated at various junctions in the gas stream inlet piping. The static pressure, temperature and velocity of the flow in the test section are approximately 1 kPa, 60 K and 720 m/s, respectively.



(a) Picture of the experimental facility.



(b) Schematic of the experimental facility, set up for an alternate configuration.

**Figure 2. Experimental Facility.**

Several different measurement techniques are used to acquire data. Schlieren imaging and Planar Laser Rayleigh Scattering (PLRS) are used to visualize the flow. Pressure taps, Particle Image Velocimetry (PIV), and Pitot probes are used to acquire more quantitative data. The PLRS imaging system is described here since it is the primary technique being used.<sup>10</sup>

Windows on both sides of the test section and transparent upper/lower walls allow optical access. Rayleigh scattering is carried out with a Nd:YAG laser (New Wave, Gemini PIV) capable of generating

approximately 100 mJ/pulse (532 nm wavelength) with 10 Hz pulse repetition. The laser beam is transformed into a thin sheet of 0.5 mm thickness using a combination of two concave cylindrical lenses (200 mm focal length) and a convex spherical lens (250 mm focal length). The laser sheet spans a plane along the centerline of the tunnel, parallel to the freestream direction. Light scattered along a direction normal to the laser sheet is captured by an unintensified CCD camera (La Vision, Imager Intense, 1376 x 1040 pixel array) instrumented with a 50 mm Nikon lens. CO<sub>2</sub> fog (solid particles) produced in the nozzle scatters laser light and evaporates under varying environments provided by primary flow features such as shockwaves and boundary layers where the local static temperature/pressure increases. CO<sub>2</sub> particles, typically 10 nm in size<sup>11</sup> form and populate the freestream, in general, in proportion to the gas density. Typical Planar Laser Rayleigh Scattering (PLRS) images are presented in Fig. 3. Figure 3(b) shows a dual shock structure with a pseudo-shock<sup>12</sup> followed by a deformed normal shock downstream. Note that these figures are a concatenation of two separate PLRS images. The dark regions show where the CO<sub>2</sub> particles have sublimated. These regions are therefore areas of higher temperature, such as boundary layers and subsonic regions after strong shocks. Shockwaves, boundary layers and turbulent flow structures are well illustrated in the two-dimensional image illuminated by the planar laser light.

Laser firing for the PLRS is synchronized with the CCD camera exposure (3  $\mu$ s shutter). One of the laser pulses is selected to trigger the jet injection module while the tunnel is operating, but delayed as desired by a pulse delay generator (SRS, DG 535) to take time-synchronized images at different phases in the flow evolution. The images are analyzed, and the location of maximum intensity is used to determine the shock location. The jet injection is controlled by a solenoid valve (ASCO, Red Hat II) driven by a controller (Optimal Engineering System Inc.) receiving its trigger signal from the delay generator.



(a) Flow with the jet off. Oblique waves can be seen emanating from the splitter plate tips. Structures in the boundary layers can also be seen.

(b) Flow with the jet on. The image shows a pseudo-shock, a deformed normal shock, and very thick, possibly separated boundary layers.

**Figure 3. Typical Rayleigh scattering images.**

## II.B. Details of the Simulations

The simulations are performed using JOE,<sup>13</sup> an unstructured, multi-physics, unsteady Reynolds-Averaged Navier-Stokes (RANS) solver. JOE is a cell-centered, finite-volume solver that is capable of supporting arbitrary polyhedral mesh elements. The steady-state calculations are performed using implicit backward Euler time integration driven by the generalized minimal residual method (GMRES) from the Portable, Extensible Toolkit for Scientific Computation (PETSc)<sup>14</sup> to solve the linear system. Unsteady, time-accurate simulations are performed using the second order backward difference formula (BDF2) with a fixed time step, again using PETSc GMRES for the inner iterations. The simulations primarily use the  $k-\omega$  shear stress transport(SST) two equation turbulence model.<sup>15</sup>

The computational mesh used for the simulations is shown in Fig. 4. To reduce the size of the computational mesh, a symmetry boundary condition is used for the plane bisecting the test section and the jet so that only half the width of the test section is simulated. This mesh consists of approximately 4 million hexahedral control volumes. Cells are concentrated in the areas around the leading edges, the boundary layers and the location of flow injection.

Two different methods were used to specify the inlet boundary conditions. The first method prescribes a flow profile that is generated by performing a separate 3D channel simulation without the splitter plates. The inlet profile is then taken as the cross-sectional plane where the simulated boundary layer thickness matches the estimated experimental boundary layer thickness. This method requires several 3D channel simulations to be carried out in order to match the velocity, boundary layer thickness, pressure and temperature. An

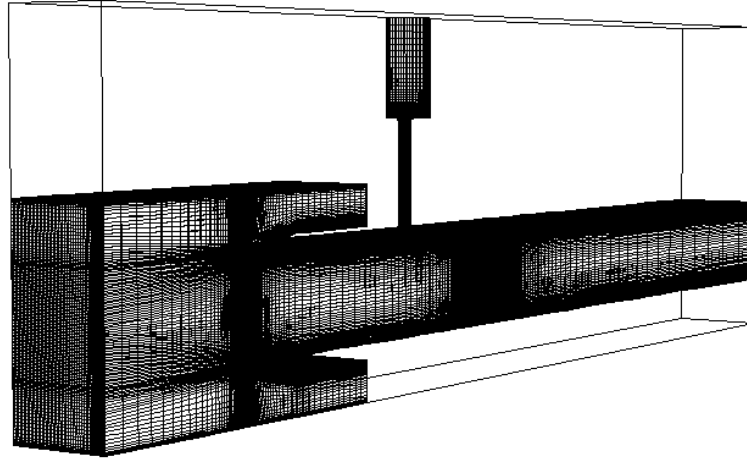


**Figure 4.** The computational mesh used for the simulations. The mesh consists of approximately 4 million hexahedral control volumes.

easier method is to construct a 3D profile using an analytic boundary layer profile,

$$u(y, z) = \min \left( u_{max} * \min \left( \left( \frac{||y| - h|}{t_{BL}} \right)^{\frac{1}{7}}, 1.0 \right), u_{max} * \min \left( \left( \frac{||z| - h|}{t_{BL}} \right)^{\frac{1}{7}}, 1.0 \right) \right), \quad (2)$$

where  $-h \leq y, z \leq h$  and  $t_{BL}$  is the boundary layer thickness. This method is used for the majority of the simulations discussed here since it allows the flow conditions to be specified directly, so that the sensitivities to these conditions can be easily obtained. The outlet boundary conditions use characteristic-based extrapolation. The tunnel walls and splitter plates are assumed to be adiabatic.

The first step in these simulations involves the computation of an initial flow solution with the jet turned off. An inviscid wall is used as the plenum boundary condition, to simulate the solenoid valve being closed. This initial flow solution is run until converged to a steady state and this solution is used to restart the simulations with the jet turned on. The converged initial flow solution is shown in Fig. 5, and can be compared to the experimental flow shown in Fig. 3(a). When the jet is turned on, the plenum boundary condition is changed to specify the pressure and flow direction.

### III. Comparison of Experimental and Computational Results

#### III.A. Jet With No Cross Flow

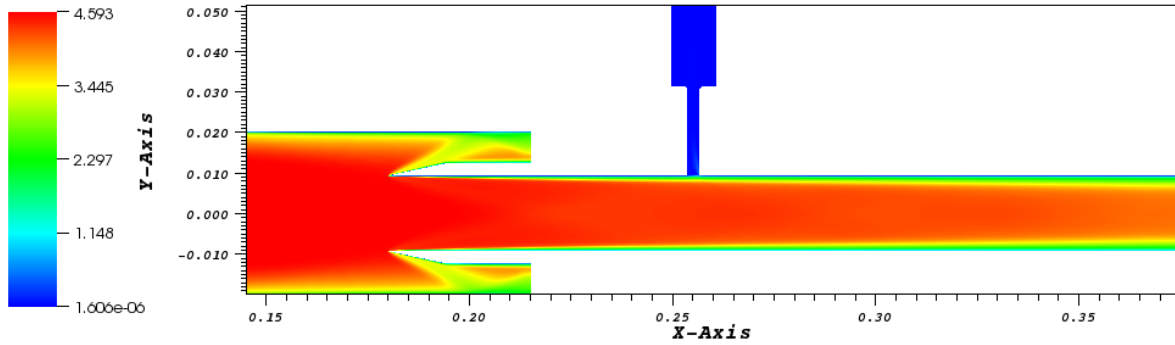
As a first step, a comparison is made for a jet of air exhausting into the configuration discussed above with no cross flow. Figure 6(a) shows a Schlieren image of an experimental run 19 ms after the valve is opened. These results are for a jet at a line pressure of 600 psi exhausting into a static tunnel at 200 torr. For these conditions, the Mach disk is located around 8.5 mm from the jet exit. For these experiments, the plenum pressure was not measured directly.

The simulations require the plenum pressure in order to specify the inflow boundary condition for the jet plenum. An experimentally derived correlation factor can be used to relate the line pressure to the plenum pressure. This is based on the Ashkenas-Sherman Correlation<sup>16</sup> relating the Mach disk height to the plenum pressure for an unconfined jet,

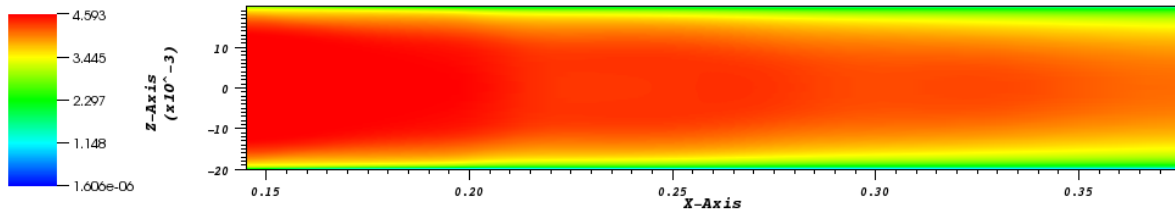
$$\frac{L_{Mach\ disk}}{d_{jet}} = 0.67 \sqrt{\frac{P_{plenum}}{P_{\infty}}}. \quad (3)$$

This correlation factor was found to be 0.257 based on earlier experiments for an unconfined jet.

Steady RANS simulations were run for several plenum pressures and the Mach disk location measured, in order to verify the value of this correlation factor. Figure 6(b) shows simulation results for a jet which produces a Mach disk at  $8.5 \pm 0.1$  mm from the jet exit, thus successfully validating the code in a simpler setting.



(a) Vertical slice along the symmetry plane.



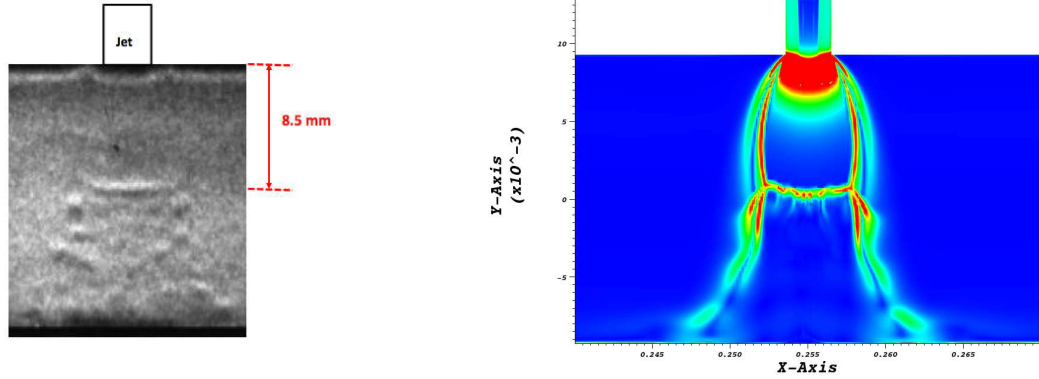
(b) Horizontal slice along the tunnel center plane.

Figure 5. Mach number contours showing the initial flow solution with the jet turned off.

### III.B. Unsteady Flow Features

Figure 7 shows several Rayleigh scattering images at different times from a typical experimental run for the full configuration. Figure 7(a) shows the flow between the splitter plates before the jet is turned on. Fairly uniform flow and thin boundary layers can be observed. Two weak oblique waves originating at the tips of the splitter plates can be seen. Figure 7(b) shows the flow 16 to 17 ms after jet injection is initiated. A shock is present in front of the jet as evidenced by the dark region, and a compression wave can be seen further upstream. The compression wave is likely a pseudo-shock. Pseudo-shocks are a result of shock wave turbulent boundary layer interactions resulting in a series of converging compression waves.<sup>12</sup> Pseudo-shocks are characterized by a sudden decrease in Mach number, as after a normal shock, but the flow is not necessarily subsonic. The Rayleigh scattering image is bright, implying that the flow downstream of the wave remains supersonic, a fact which was also confirmed by the simulations. The boundary layers are dramatically thicker after this compression wave, indicating that they are highly turbulent and may have separated. This compression wave quickly moves further upstream until it reaches the position shown in Fig. 7(c), where it remains for 36 ms. Less than a millisecond later, the compression wave abruptly moves upstream and out of the inlet and the system unstarts, as seen in Fig. 7(d). The exact cause for this sudden unstart is still unknown. One theory is that there is a slow buildup of pressure during the 36 ms that the pseudo-shock is stationary that reaches some critical threshold at 55 ms. This theory will be tested when the pressure tap measurements are available, assuming a similar phenomenon is observed when the spacing between the splitter plates is reduced.

Unsteady, time-accurate simulations produce qualitatively-similar flow structures. Quantitative comparisons can not be made since these particular time-accurate simulations were run at Mach 4.3 instead of Mach 4.6. Figures 8 and 9 show Mach number snapshots from the time-accurate unsteady RANS simulation. Figures 8(a) and 9(a) show the Mach number along the center plane of the tunnel. These plots show that the structure of the flow fields compare well, despite the discrepancies in operating conditions between the experiment and simulation. Figures 8(b) and 9(b) show the Mach number along the center plane of the tunnel. The pseudo-shock downstream of the isolator tips is captured, as is the shock, with subsonic flow behind it, immediately in front of the jet. The shocks are accompanied by separated boundary layers. There is a large separated region along the sidewall, and smaller separated regions along the splitter plates.



(a) Schlieren image for line pressure of 600 psi.

(b) Density gradient for plenum pressure of 800 kPa.

**Figure 6.** Experimental and computational results for a jet exhausting into a 200 torr static tunnel. The Mach disk location for each case is around 8.5 mm from the jet exit.

### III.C. Unstart Margin Results

While it is encouraging that the overall flow features are represented, the goal of this work is to determine the accuracy and variability of the prediction of the unstart margins. This is accomplished by varying the strength of the jet and determining the location of the leading shock relative to the leading edge of the splitter plates. The steady-state flow fields for simulations run using two different plenum pressures are shown in Figs. 11 and 12. These plots show the Mach number variation along the symmetry plane, as in Fig. 12(a), and the horizontal plane through the center of the test section, as in Fig. 12(b), for a 600 kPa jet. The Mach number along the centerline of the tunnel for these simulations is plotted in Fig. 13. From these plots, the shock location is determined relative to the jet centerline. The shock location for the experimental runs is determined by analyzing the PLRS images and determining the location of maximum intensity as shown in Fig. 14. The splitter plate tips are 75 mm from the jet centerline and serve as the definition of the unstart boundary. The distance from the unstart boundary provides an indication of the operability margin of the system. This data is collected for multiple plenum pressures and used to form an unstart margin curve. The results of these experiments and the simulations under the assumed nominal conditions are shown in Fig. 10.

Recent experimental runs have measured the plenum pressure directly. Based on these new results, the line pressure can be related to the plenum pressure using the formula

$$P_{plenum} = 0.2631 * P_{line} + 1.1964, \quad (4)$$

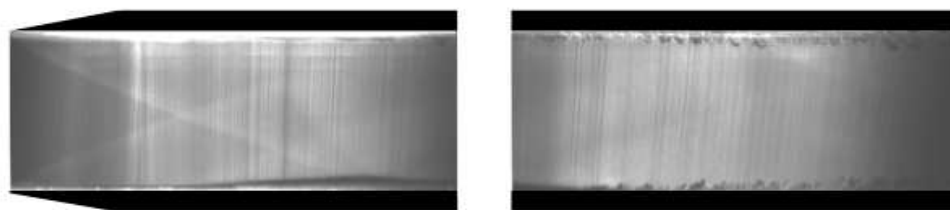
where  $P_{plenum}$  and  $P_{line}$  are measured in psi. This conversion is used to place the experimental results on the same plot as the simulations, rather than the earlier factor. Any errors in this conversion will shift the experimental data to the left or right, and will have a direct impact on how well the results compare.

There is a large difference in shock position between the experimental results and the simulations. There are several possible reasons for this discrepancy. A number of assumptions and approximations are required to interpret the experimental results or perform a simulation. These assumptions and approximations introduce errors and uncertainties in the results, and may explain the differences between the experiment and simulations under the nominal conditions. Several sources of error and uncertainty have been identified. The effects of these errors and uncertainties are explored in the next section.

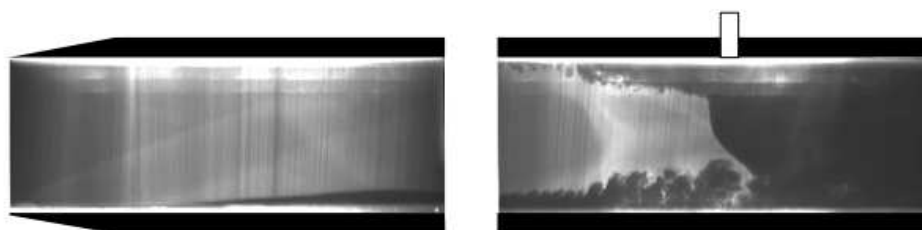
## IV. Sources of Error and Uncertainty

### IV.A. Knowledge of Flow Conditions

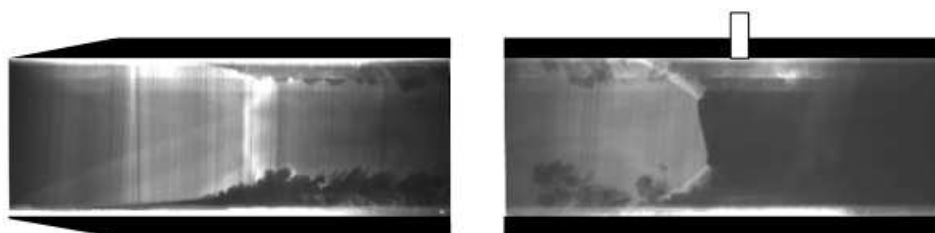
The values of the flow velocity, pressure, temperature, boundary layer thickness and turbulence quantities at the inflow boundary need to be specified as inputs to the simulations. The undisturbed velocity in the test section was measured using PIV and specified as  $720 \text{ m/s} \pm 10 \text{ m/s}$ . The flow Mach number was determined using a wedged shape probe placed at several locations spanning the height of the tunnel and measuring



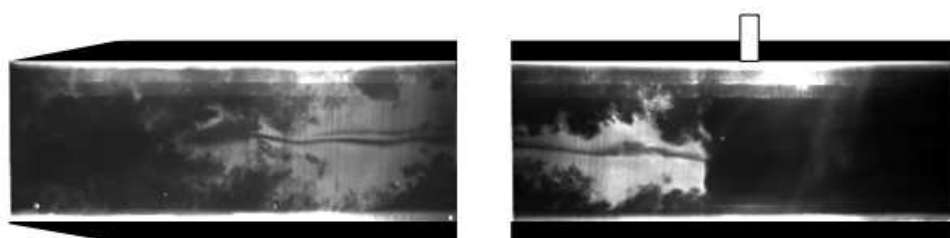
(a) Before jet injection.



(b) 16 to 17 ms after jet injection.

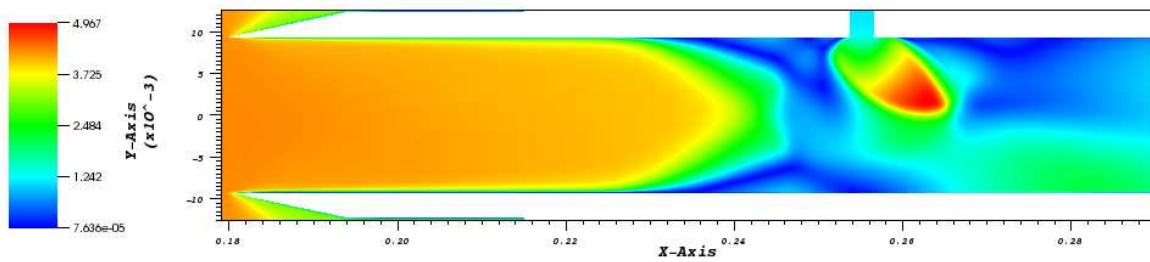


(c) 18 to 54 ms jet injection.

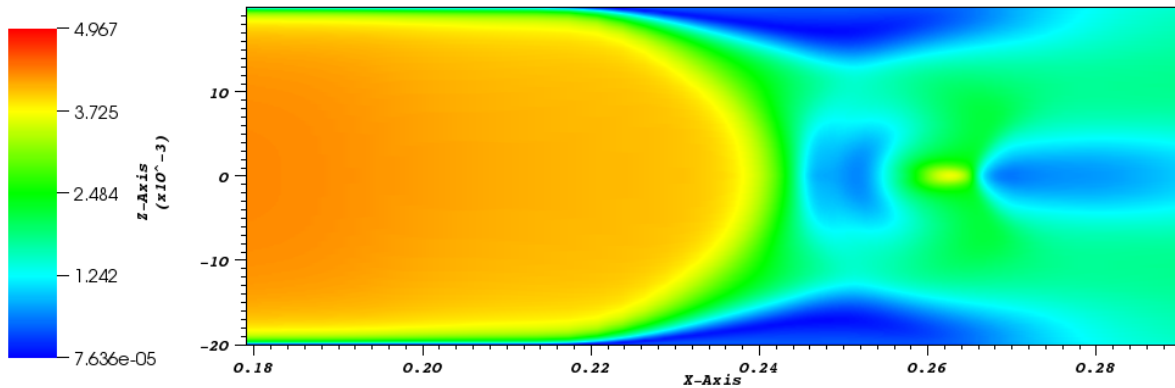


(d) Unstart 55 ms after jet injection.

Figure 7. Rayleigh scattering images showing the flow field at several time instances before and after unstart.

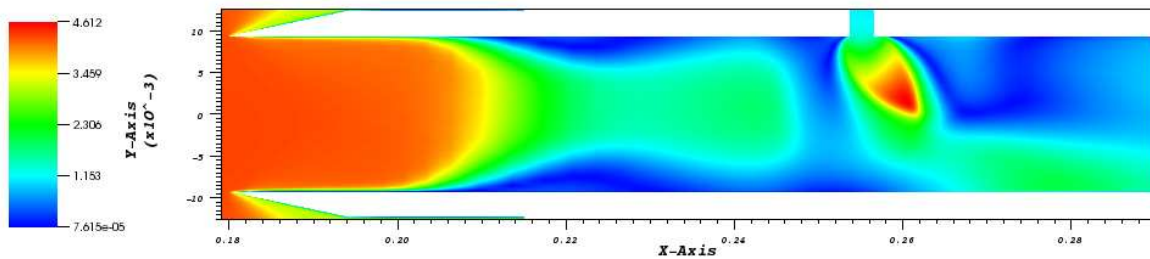


(a) Vertical slice along the symmetry plane.

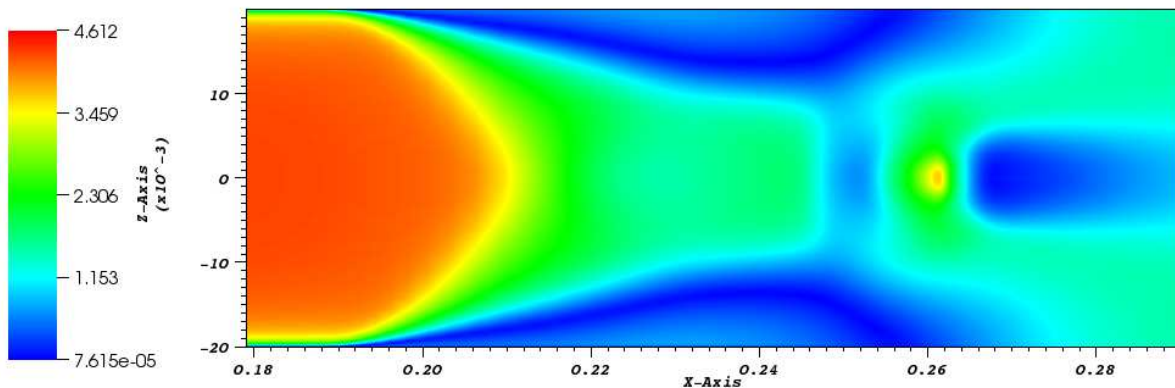


(b) Horizontal slice along the tunnel center plane.

Figure 8. Mach number plots from the time-accurate unsteady RANS simulations showing that the flow structures are similar to the experimental results shown in Fig. 7(b). Slices along the symmetry plane and center plane of the tunnel are shown.



(a) Vertical slice along the symmetry plane.



(b) Horizontal slice along the tunnel center plane.

Figure 9. Mach number plots from the time-accurate unsteady RANS simulations showing that the flow structures are similar to the experimental results shown in Fig. 7(c). Slices along the symmetry plane and center plane of the tunnel are shown.

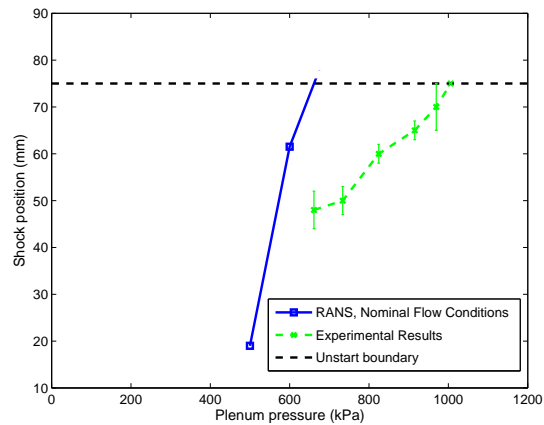
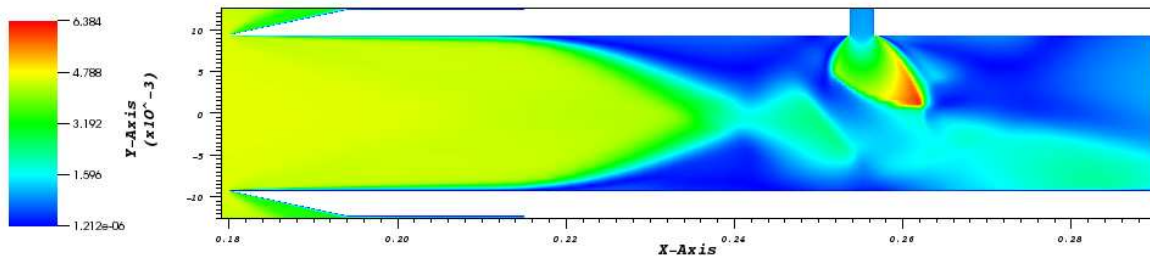
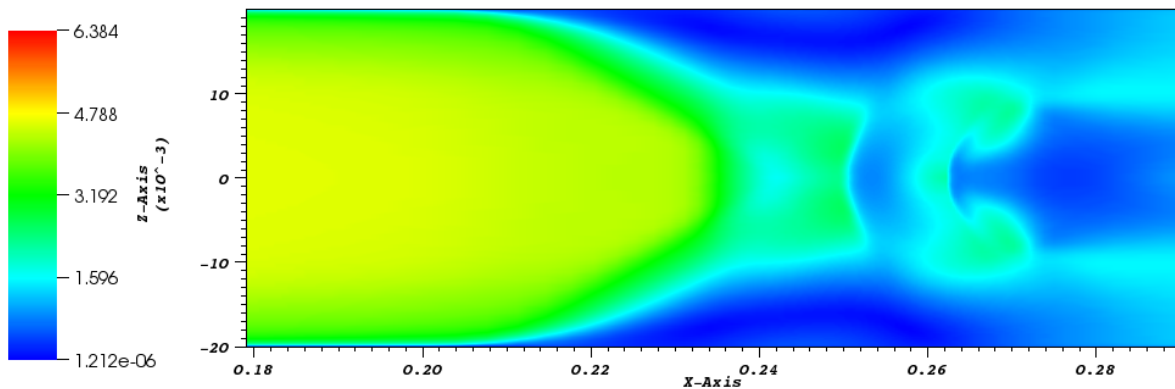


Figure 10. Shock location versus plenum pressure. This figure shows both the experimental results and the simulations at the nominal flow conditions. Unstart occurs when the shock location moves upstream of the tips of the splitter plates, 75 mm from the center of the jet exit.

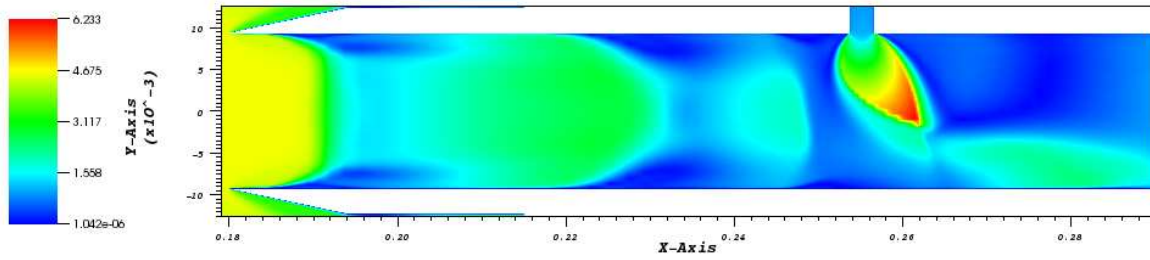


(a) Vertical slice along the symmetry plane.

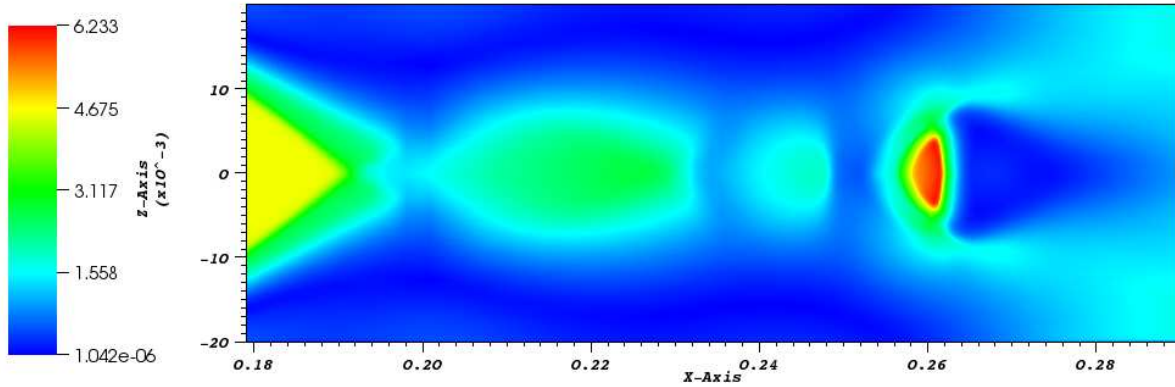


(b) Horizontal slice along the tunnel center plane.

Figure 11. Simulation under nominal inflow conditions for a plenum pressure of 500 kPa, showing the Mach number variation.

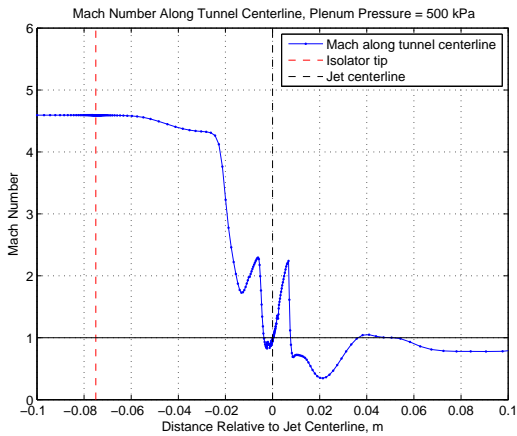


(a) Vertical slice along the symmetry plane.

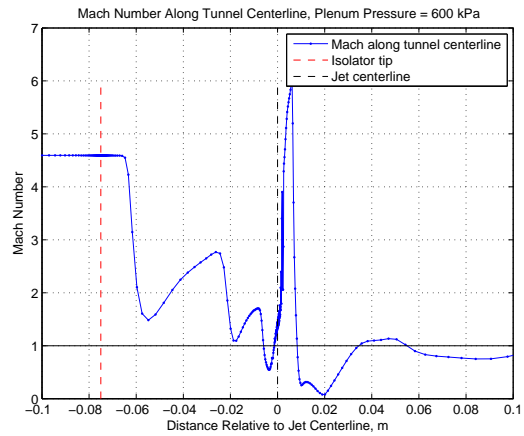


(b) Horizontal slice along the tunnel center plane.

Figure 12. Simulation under nominal inflow conditions for a plenum pressure of 600 kPa, showing the Mach number variation.



(a)  $P_{plenum} = 500$  kPa.



(b)  $P_{plenum} = 600$  kPa.

Figure 13. Mach number along the centerline of the tunnel for several jet plenum pressures at the nominal inflow conditions. These plots are used to determine the shock location. The shock location is taken as the midpoint of the first sharp decrease in Mach number.

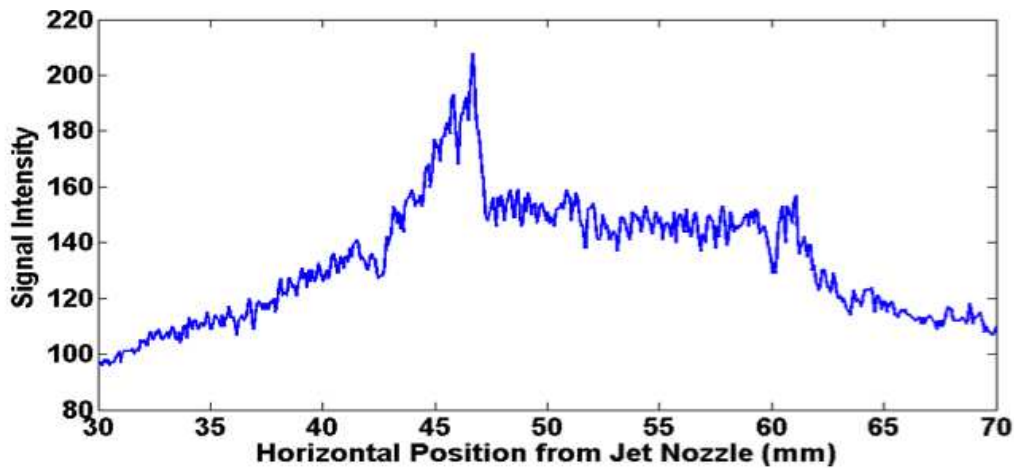


Figure 14. Intensity level of the PLRS image. The maximum intensity is the location of the pseudo-shock.

the oblique shock angle. The angle of the wedge and the oblique shock angle were then used to determine the Mach number of the flow. Based on these measurements, the flow Mach number was taken as  $4.6 \pm 0.2$  along the height of the channel.

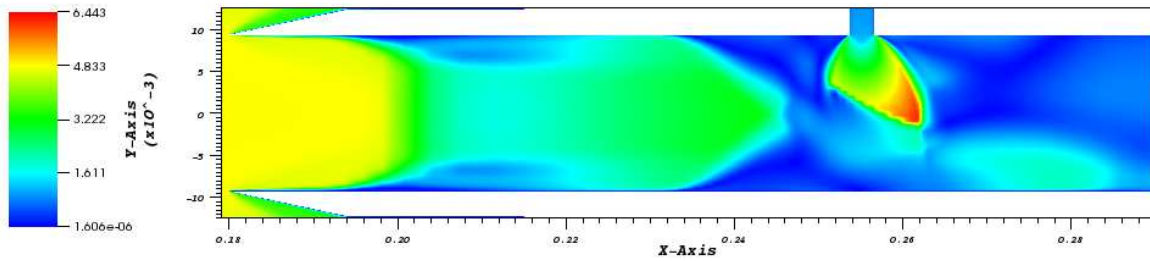
Boundary layer thickness measurements are currently underway using Pitot probes. Based on these preliminary measurements, the boundary layer is approximately 11 mm thick at a location 20 mm downstream of the isolator tip. For the simulations, a boundary layer thickness of 7 mm is specified at the inflow boundary of the mesh, which grows to approximately match the experimental results.

The temperature can be calculated by either using the velocity and Mach number results or by assuming isentropic expansion to the measured Mach number. The pressure is also determined by assuming an isentropic expansion. Based on these calculations, the nominal conditions of the flow are estimated to be 720 m/s at a temperature of 60 K and a pressure of 1 kPa.

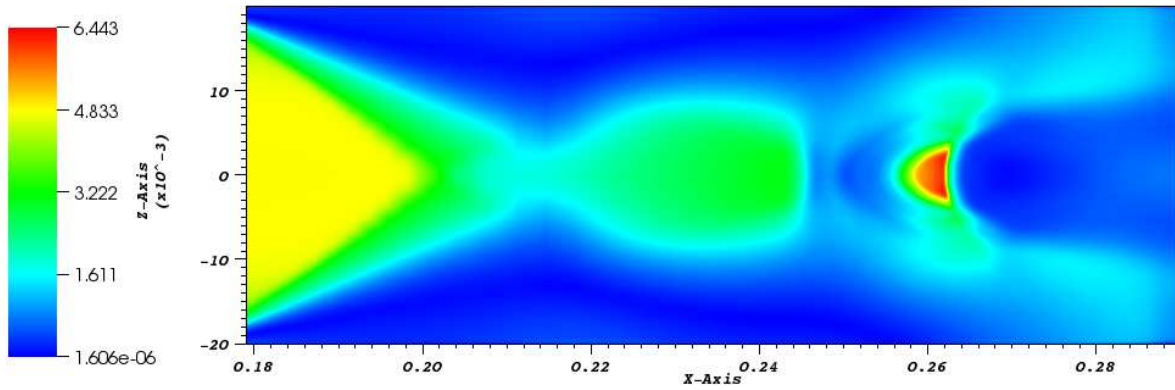
The extreme values for velocity and Mach number can be used to obtain a range of temperatures by assuming the gas is air. Following this approach, the temperature range was determined to be 54 K to 68 K. Figure 15 shows the steady-state flow for a plenum pressure of 600kPa when the temperature is lowered to 54 K and the other flow quantities are held at their nominal values. This figure can be contrasted with the flow field produced by the same plenum pressure at the nominal flow conditions shown in Fig. 12. With the lowered temperature, the shock system is further downstream compared to the nominal case meaning that it is farther from unstating. By lowering the temperature, the momentum of the crossflow is increased, lowering the jet momentum ratio, Eq. (1). An equivalent effect can be achieved by changing the pressure or flow velocity.

The effect of decreasing the jet momentum ratio by changing the properties of the crossflow from its nominal values is shown in Figs. 16(a) and 16(b). The magnitudes of these perturbations are chosen to produce the same jet momentum ratio. As such, the three perturbations all have a similar effect on the shock location. The perturbed value of pressure is 1111 Pa, an 11% increase in pressure over the nominal value. The perturbed value of the flow velocity is 759 m/s, a 5.4% increase over the nominal value.

The movement of the pseudo-shock is accompanied by separated boundary layers. There is a large separated region on the sidewalls, and smaller separated regions on the splitter plates. This is shown in Fig. 17, which shows Mach number vector plots corresponding to the 54K simulations shown in Fig. 15. A reasonable conjecture is that the thickness of the sidewall boundary layer would have a significant impact on the shock location. Thicker boundary layers could shift the shock location upstream. The effect of boundary layer thickness on the unstart margin is investigated by simulating the flow with a series of specified boundary layer thicknesses, as shown in Fig. 18. These simulations seem to suggest that for a wide range of thicknesses, the boundary layer on the sidewall has a negligible impact on the predicted margin. This is a surprising result, and it is only at the largest thickness investigated that an effect can be seen. In this extreme situation, however, the flow between the splitter plates is contaminated by the top and bottom wall boundary layers.

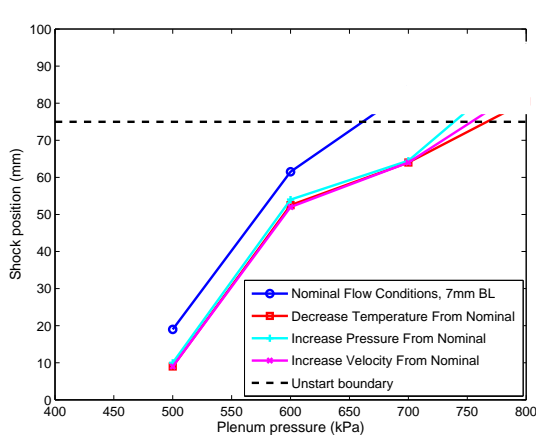


(a) Vertical slice along the symmetry plane.

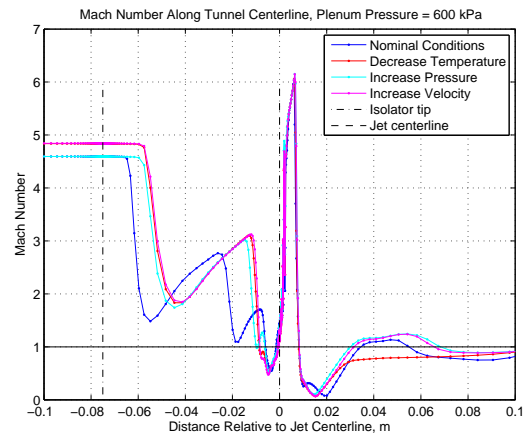


(b) Horizontal slice along the tunnel center plane.

Figure 15. Simulation with inflow temperature decreased from 60K to 54K for a plenum pressure of 600 kPa.

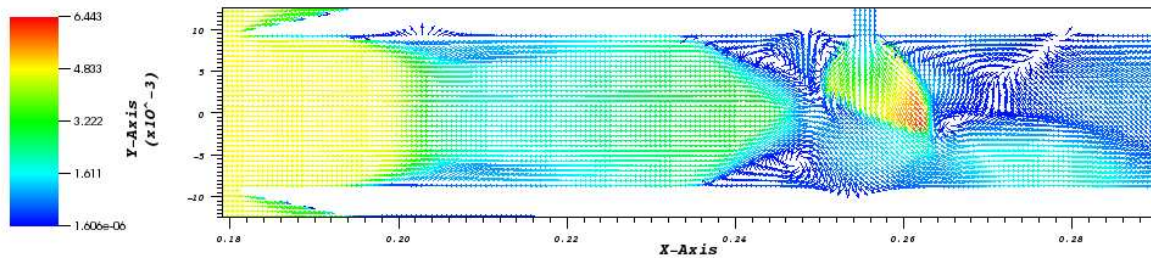


(a) Shock location versus plenum pressure.

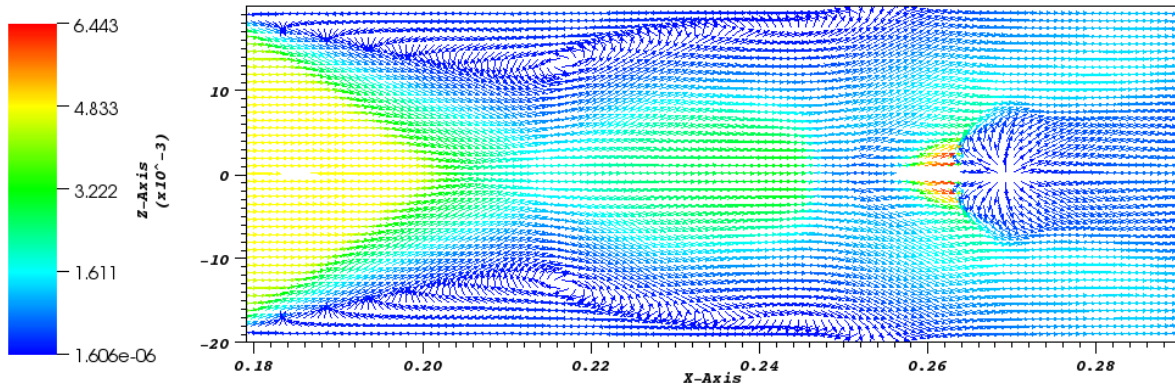


(b) Mach number along the tunnel centerline for simulations with a plenum pressure of 600 kPa.

Figure 16. This figure shows effects of perturbing the inflow conditions from their nominal values. The magnitudes of the perturbations were chosen to produce the same jet momentum ratio, and should therefore have similar impacts.

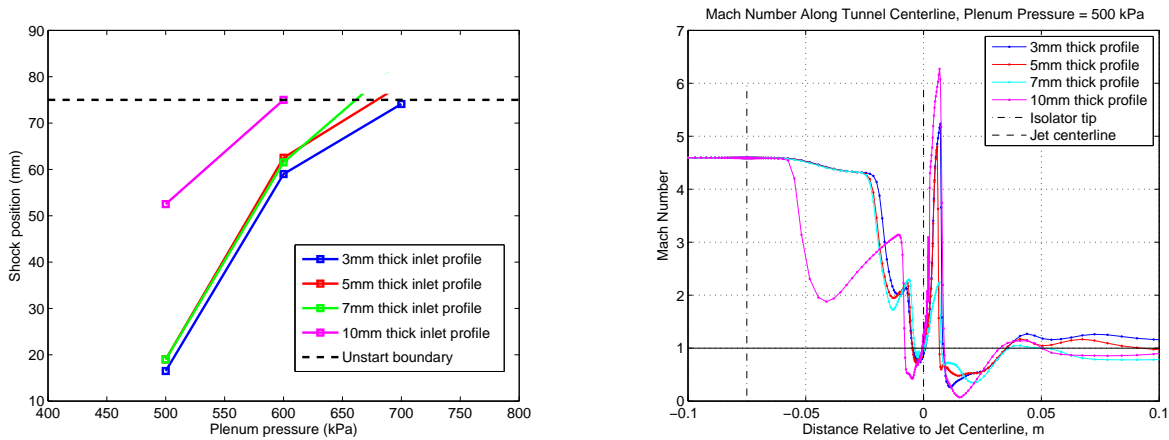


(a) Vertical slice along the symmetry plane.

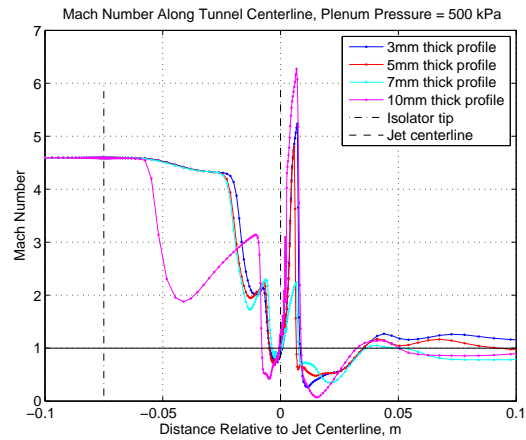


(b) Horizontal slice along the tunnel center plane.

Figure 17. Mach number vector plots for the simulation at a temperature of 54K with a plenum pressure of 600 kPa. These plots show that downstream of the pseudo-shock there is a large region of separated flow on the side walls of the tunnel, and smaller regions on the splitter plates.



(a) Shock location versus plenum pressure.



(b) Mach number along the tunnel centerline for simulations with a plenum pressure of 500 kPa.

Figure 18. A comparison of the effect of boundary layer thickness on the simulations. There is little effect as long as the boundary layers are thin enough that the splitter plates are able to isolate the core flow.

#### IV.B. Knowledge of the Physics of the Flow

Two basic assumptions are made about the physics of the flow that are inherent in both the simulations and experiment. In addition to these basic assumptions, the simulations make additional approximations to make the problem computationally tractable.

The first basic assumption is that the flow is in the continuum flow regime. This is required in order to describe the flow using the Navier-Stokes equations. This influences the type of simulation that can be

used and the fundamental equations that are used to analyze the experimental results. The assumption of continuum flow may, however, not be entirely valid. There are discrepancies in the angle of the oblique wave originating at the tip of the splitter plate on the flat side of the plate. Figure 19 shows the oblique wave seen in the experimental runs. The observed angle is approximately twice the expected Mach wave angle. A possible explanation for this discrepancy could be that there is a small region near the tip of the splitter plate that is behaving as a rarefied gas.<sup>17</sup> Another possible explanation has to do with imperfections in the geometry of the system and will be discussed in a later section.



**Figure 19.** A PLRS image showing the oblique wave emanating from the tip of the splitter plate. The angle of this wave is greater than expected, which may be due to geometric imperfections or rarefied gas effects.

The second basic assumption is that the fluid behaves as a gas for which properties such as the ratio of specific heats,  $\gamma$ , and the specific gas constant,  $R$ , can be defined. Throughout the simulations, and for many other calculations, the properties of air are used. The fluid is actually a mixture of air and  $\text{CO}_2$ , with the latter accounting for approximately 25% by volume. It is certainly possible to determine the properties for a mixture of gases, however, at the nominal flow conditions in the test section the  $\text{CO}_2$  is a solid. A simplifying assumption is that the solid particles convect with the flow without affecting it. Under this assumption the fluid can be treated as simply air, but the assumption may not be entirely valid. The reason for using  $\text{CO}_2$  is to image the flow by illuminating the solid  $\text{CO}_2$  particles. The  $\text{CO}_2$  particles sublime in the higher temperature regions of the flow such as boundary layers and subsonic regions. This creates regions where the image is dark, allowing these flow structures to be visualized. This also means that in these regions the fluid is a multiphase mixture of gases. To further complicate the situation, the change of phase from solid to gas may absorb energy from the flow and alter the flow field.

Because of general non-equilibrium flow phenomena near the injector and in the shock-boundary layer interactions, RANS models can be expected to suffer from large errors. The nominal simulations use the  $k-\omega$  shear stress transport(SST) two equation turbulence model.<sup>15</sup> Figure 20 shows the effect of choosing a difference turbulence model, namely the Spalart-Allmaras model.<sup>18</sup> This choice is shown to have a significant impact on the unstart margin prediction. Using the Spalart-Allmaras model, the shock locations are predicted to be further upstream than for the  $k-\omega$  SST model for the same plenum pressure and nominal flow conditions.

#### IV.C. Knowledge of the Geometry of the Experiment

When analyzing an experiment or running a simulation, an idealized geometry is used that may not be truly representative of the actual physical system. The actual dimensions of the system depend on the tolerances of the machining process used to make the components. For instance, the corner radius of the plenum is specified as  $1 \text{ mm} \pm 0.2 \text{ mm}$ . There may also be slight misalignments when combining the various components forming the inlet in the wind tunnel. The splitter plates should be oriented at  $0^\circ$  to the horizontal but the uncertainty in this angle is estimated to be approximately  $\pm 0.5^\circ$ . There may also be deformations as a result of repeated use of the system. Splitter plates with  $10^\circ$  tips were used at one point, but after repeated runs, the tips bowed outward due to the high pressures associated with unstart. It is possible that the  $12^\circ$  splitter plates may also deform given the right conditions. These deviations from the idealized geometry can have a dramatic influence on the results of the experiment. Another possibility is that the actual geometry may deviate from the idealized geometry. The splitter plate tips are assumed to be perfectly sharp,  $12^\circ$  angles. In reality, the tip may be blunted and the plates may be machined at a slightly different angle. Also, the splitter plates may not be perfectly parallel to each other and the flow.

Aside from the uncertainties in the geometry discussed above, there is a known difference between the actual geometry and the simulated geometry. Currently, the experiments use an 11 mm diameter plenum

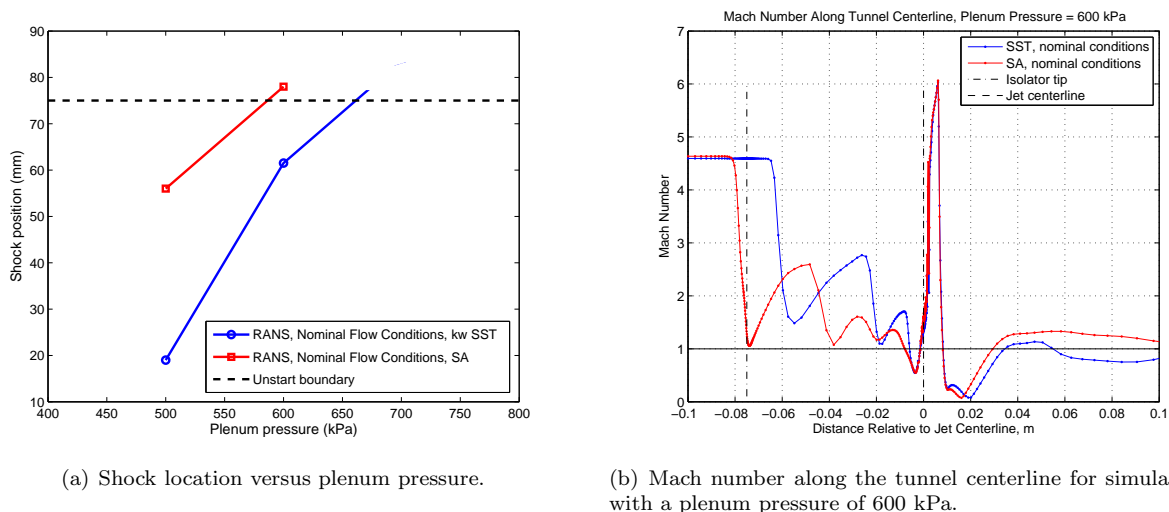


Figure 20. A comparison between simulations using the  $k-\omega$  SST and the Spalart-Allmaras(SA) turbulence models at the same nominal conditions.

with the junction between the bottom of the plenum and the tube connecting the plenum to the tunnel having a 1 mm corner radius. This plenum allows the plenum pressure to be measured directly. The simulations also use this plenum geometry. However, the experimental results we are comparing to used a 10.5 mm diameter plenum, and the junction was not rounded.

The effect of the plenum geometry on the shock location is explored by comparing simulations for three plenum diameters with straight corners to the 11 mm plenum with a rounded corner. Figure 21 shows the four plenums that were simulated. Figure 21(b) shows the plenum used to produce the experimental results presented here. Figure 21(d) shows the plenum that is currently used in the experiments and is used for the simulations. The rounding of the corner has a noticeable impact on the flow leaving the plenum. It was anticipated that the dominant effect would be from the plenum diameter. Figure 22(a) shows the effect of the plenum geometry on the unstart margin curve. The rounding of the corner has a dramatic impact on the unstart margin curve, but the diameter of the plenum appears to have very little effect. Figure 22(b) shows the Mach number variation along the centerline of the tunnel. As can be seen, the diameter of the plenum does impact the shock location. However, the rounded corner has a much larger impact on the shock location and the diameter is a secondary effect.

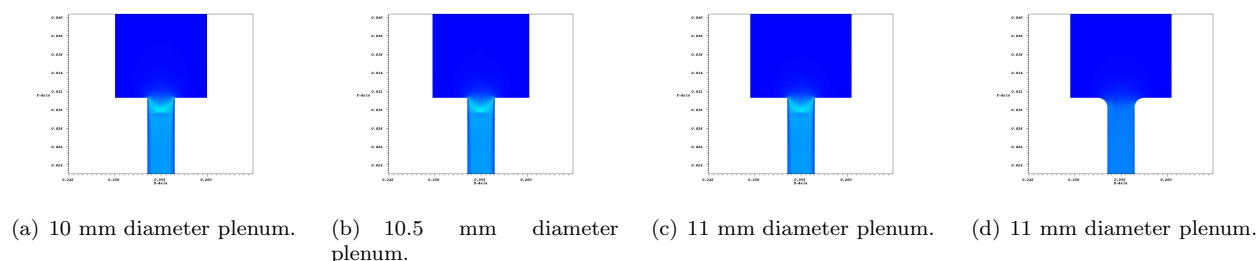
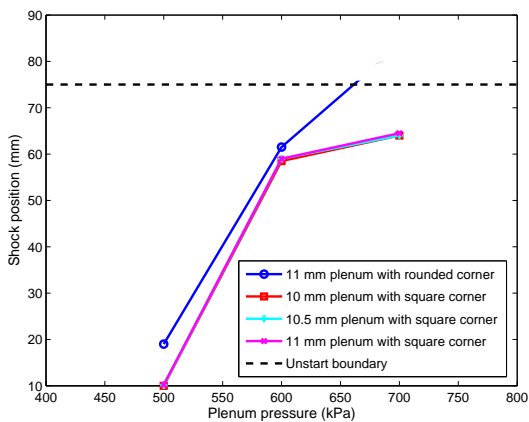


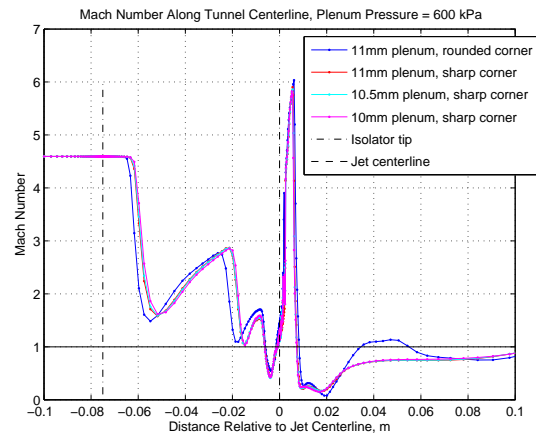
Figure 21. Four different plenum geometries used to investigate the impact of diameter and corner radius on the shock location. These pictures show the Mach number of the flow as it leaves the plenum.

## V. Conclusions and Continuing Work

A preliminary investigation of unstart due to mass injection has been conducted using both experiments and simulations. For a jet with no cross flow in confined conditions, the simulations predict the correct Mach disk height. For the unstart experiments, the simulations produce qualitatively similar flow features, but there exist significant discrepancies in the predictions for the conditions under which unstart is initiated. These discrepancies may be related to the uncertainties inherent in the system. The sources of uncertainty



(a) Shock location versus plenum pressure.



(b) Mach number along the tunnel centerline for simulations with a plenum pressure of 600 kPa.

**Figure 22.** A comparison between simulations using the four different plenum geometries shown in Fig. 21. Whether the plenum has a square or rounded corner has a significant impact on the shock location. The diameter of the plenum is a secondary effect.

can be separated into three categories: knowledge of the physics of the flow, knowledge of the geometry of the experiment, and knowledge of the flow conditions.

Several of these uncertainties have been investigated individually, and have been shown to have varying levels of impact on the unstart margin curve. The boundary layer thickness along the walls of the tunnel is shown to have a negligible effect. The inflow conditions can have a significant effect, depending on the magnitude of the perturbation from the nominal conditions. The plenum geometry has a measurable influence in that the primary effect is from whether the corner is rounded or square, while the diameter of the plenum is a secondary effect. The choice of turbulence model has a very significant impact on the unstart margin curve. Several of these effects could be combined in some way to match the experimental data. However, the goal of this work is not to match the experiment exactly, but to quantify the effect of uncertainties on the predictive simulation with enough confidence that the experimental results lie inside these error bars.

Efforts are currently underway to explore these uncertainties in more detail and perform more detailed uncertainty quantification. Modifications to the experiment are also under way that should aid in this effort. The static pressure is presently being measured at several locations along the jet-side splitter plate using pressure taps. Future experiments will vary the concentration of  $\text{CO}_2$  to assess this effect on unstart. This will eventually include performing the experiment with no  $\text{CO}_2$  and relying on the pressure measurements.

The simulations will expand upon this preliminary work in order to perform a more formal uncertainty quantification study. This will include sampling the uncertainties from a distribution rather than simply using upper and lower bounds, and exploring the combined effects of multiple uncertainties. Additional time-accurate, unsteady simulations will be performed to further validate the use of the steady simulations for predictions of unstart, and allow quantitative comparisons with the experimental pressure trace measurements. Finally, a rigorous study of grid convergence and turbulence model variability will be conducted.

## Acknowledgments

This work was funded by the United States Department of Energy's Predictive Science Academic Alliance Program (PSAAP) at Stanford University.

## References

<sup>1</sup>Karl, S., Hannemann, K., Mack, A., and Steelant, J., "CFD Analysis of the HyShot II Scramjet Experiments in the HEG Shock Tunnel," *AIAA paper 2008-2548*, 15th AIAA International Space Planes and Hypersonic Systems and Technologies Conference, 2008.

<sup>2</sup>Voland, R. T., Huebner, L. D., and McClinton, C. R., "X-43A Hypersonic vehicle technology development," *Acta Astronautica*, Vol. 59, No. 1-5, 2006, pp. 181 – 191, Space for Inspiration of Humankind, Selected Proceedings of the 56th International

Astronautical Federation Congress, Fukuoka, Japan, 17-21 October 2005.

<sup>3</sup>Hank, J., Murphy, J., and Mutzman, R., "The X-51A Scramjet Engine Flight Demonstration Program," *AIAA paper 2008-2540*, 15th AIAA International Space Planes and Hypersonic Systems and Technologies Conference, 2008.

<sup>4</sup>Jackson, K., Gruber, M., and Barhorst, T., "The HIFiRE Flight 2 Experiment: An Overview and Status Update," *AIAA paper 2009-5029*, 45th AIAA/ASME/SAE/ASEE Joint Propulsion Conference and Exhibit, 2009.

<sup>5</sup>Gruber, M., Jackson, K., Eklund, D., Barhorst, T., Hass, N., Storch, A., and Liu, J., "Instrumentation and Performance Analysis Plans for the HIFiRE Flight 2 Experiment," *AIAA paper 2009-5032*, 45th AIAA/ASME/SAE/ASEE Joint Propulsion Conference and Exhibit, 2009.

<sup>6</sup>Smart, M. K. and Suraweera, M. V., "HIFiRE 7 - Development of a 3-D Scramjet for Flight Testing," *AIAA paper 2009-7259*, 16th AIAA/DLR/DGLR International Space Planes and Hypersonic Systems and Technologies Conference, 2009.

<sup>7</sup>Mashio, S., Kurashina, K., Bamba, T., Okimoto, S., and Kaji, S., "Unstart Phenomenon Due to Thermal Choke in Scramjet Module," *AIAA paper 2001-1887*, 10th AIAA/NAL-NASDA-ISAS International Space Planes and Hypersonic Systems and Technologies Conference, 2001.

<sup>8</sup>Do, H., Im, S.-k., Mungal, M., and Cappelli, M., "The influence of boundary layers on supersonic inlet flow unstart induced by mass injection," *Experiments in Fluids*, 2011, pp. 1–13, 10.1007/s00348-011-1077-3.

<sup>9</sup>Smith, S. H. and Mungal, M. G., "Mixing, structure and scaling of the jet in crossflow," *Journal of Fluid Mechanics*, Vol. 357, No. -1, 1998, pp. 83–122.

<sup>10</sup>Do, H., Im, S.-k., Mungal, M., and Cappelli, M., "Visualizing supersonic inlet duct unstart using planar laser Rayleigh scattering," *Experiments in Fluids*, Vol. 50, 2011, pp. 1651–1657, 10.1007/s00348-010-1028-4.

<sup>11</sup>Miles and, R. B. and Lempert, W. R., "Quantitative Flow Visualization in Unseeded Flows," *Annual Review of Fluid Mechanics*, Vol. 29, No. 1, 1997, pp. 285–326.

<sup>12</sup>Sugiyama, H., Tsujiguchi, Y., and Honma, T., "Structure and Oscillation Phenomena of Pseudo-Shock Waves in a Straight Square Duct at Mach 2 and 4," *AIAA paper 2008-2646*, 15th AIAA International Space Planes and Hypersonic Systems and Technologies Conference, 2008.

<sup>13</sup>Pecnik, R., Terrapon, V. E., Ham, F., and Iaccarino, G., "Full system scramjet simulation," *Annual Research Briefs, Center for Turbulence Research, Stanford University*, 2009.

<sup>14</sup>Balay, S., Brown, J., , Buschelman, K., Eijkhout, V., Gropp, W. D., Kaushik, D., Knepley, M. G., McInnes, L. C., Smith, B. F., and Zhang, H., "PETSc Users Manual," Tech. Rep. ANL-95/11 - Revision 3.1, Argonne National Laboratory, 2010.

<sup>15</sup>Menter, F. R., "Two-Equation Eddy-Viscosity Turbulence Models for Engineering Applications," *AIAA Journal*, Vol. 32, No. 8, 1994, pp. 1598–1605.

<sup>16</sup>Ashkenas, H. and Sherman, F. S., "The Structure and Utilization of Supersonic Free Jets in Low Density Wind Tunnels," *Rarefied Gas Dynamics, Volume 2*, edited by J. H. de Leeuw, 1965, pp. 84–+.

<sup>17</sup>Lofthouse, A. J. and Boyd, I. D., "Hypersonic Flow over a Flat Plate: CFD Comparison with Experiment," *AIAA paper 2009-1315*, 47th AIAA Aerospace Sciences Meeting, 2009.

<sup>18</sup>Spalart, P. R. and Allmaras, S. R., "A one-equation turbulence model for aerodynamic flows," *La Recherche Aeronautique*, Vol. 1, No. 1, 1994, pp. 5–21.